IEEE Access
Multidisciplinary | Rapid Review | Open Access Journal

Received September 14, 2017, accepted October 24, 2017, date of publication November 8, 2017,
date of current version December 22, 2017.

Digital Object Identifier 10.1109/ACCESS.2017.2771204

Vehicle System State Estimation Based on Adaptive Unscented Kalman Filtering Combing With Road Classification

ZHENFENG WANG, (Student Member, IEEE), YECHEN QIN, (Member, IEEE), LIANG GU, AND MINGMING DONG

School of Mechanical Engineering, Beijing Institute of Technology, Beijing 100081, China

Corresponding author: Mingming Dong (vdmm@bit.edu.cn)

This work was supported in part by the National Natural Science Foundation of China under Grant U1564210, in part by the Innovative Talent Support Program for Post-Doctorate of China under Grant BX201600017, in part by the China Post-Doctoral Science Foundation under Grant 2016M600934, and in part by the China Scholarship Council under Grant 201706030029.

ABSTRACT This paper presents a new method to address issues associated with vehicle system state estimation using an unscented Kalman filter (UKF) with considering full-car system and nonlinear tire force under various international standards organization (ISO) road conditions. Due to the fact that practical road information is complex and noise covariance cannot be treated as a constant, the influence of varying vehicle system process noise variance and measurement noise covariance on the estimation accuracy of the UKF is first discussed. To precisely estimate road information, a novel road classification method using measured signals (vertical acceleration of sprung mass and unsprung mass) of vehicle system is proposed. According to road excitation levels, different road process variances are defined to tune the vehicle system's variance for application of UKF. Then, road classification and UKF are combined to form an adaptive UKF (AUKF) that takes into account the relationship of different road process noise variances and measurement noise covariances under varying road conditions. Simulation results reveal that the proposed AUKF algorithm has higher accuracy for state estimation of a vehicle system under various ISO road excitation condition.

INDEX TERMS State estimation, AUKF, process noise variance, measurement noise covariance, vehicle system.

I. INTRODUCTION

Vehicle dynamics control system plays an important role in vehicle performance. Control systems such as active suspension control system (ASC), active yaw control system (AYC) and active front steering system (AFS) are especially useful in improving the ride comfort and road handling [1]–[3]; However, some vehicle state such as sprung mass velocity, unsprung mass velocity and roll rate are not easily obtained in current vehicle control system. Closed-loop implementations require a large amount of sensors, which make such systems commercially unattractive due to the cost associated with the sensors required. Accurate estimation of unmeasurable states for controllable vehicle systems is critical to the success of such systems and would reduce costs for economy cars [4]. Furthermore, accuracy of state estimation has a significant effect on control. To accurately acquire state of a vehicle system, many linear and nonlinear filtering approaches have been utilized [5]–[8]. Among them, Kalman Filter (KF) is among the most commonly used approaches to estimate vehicle system state.

In 1960s, Kalman [9] first presented the KF approach to solve discrete-time linear filtering problems. This method has been widely applied in the field of vehicle system due to its ability to provide optimal solutions and fast convergence in a noisy environment. However, traditional KF can only deal with linear systems. Vehicle systems are typically a nonlinear system (e.g. spring stiffness, nonlinear tire force and nonlinear damping ratio). As a result, improved methods have been proposed for nonlinear filtering, such as extended Kalman filter (EKF) and Unscented Kalman Filter (UKF). Leung *et al.* [10] proposed an extended kinematic Kalman filter (EKKF) with fuzzy logic control to estimate the vehicle state. Results showed that higher accuracy was obtained using the proposed method. Huang *et al.* [11] utilized EKF and adaptive Kalman filter (AKF) to estimate a center of gravity (C.G.) position for lightweight vehicles in real time.

Experimental results indicated that the proposed method achieved acceptable accuracy in estimating C.G. position. Li *et al.* [12] proposed a new variable structure extended Kalman filter integrated with a sideslip angle rate feedback algorithm and damping to estimate sideslip angle on a road with low friction. Results indicated that the proposed method provided accurate sideslip angle to some extent for vehicle stability control under a low friction road. Hong *et al.* [13] used EKF and UKF to identify vehicle inertial parameters. While, EKF required analytical linearization of the vehicle model, UKF approximated parameter distribution with discrete sigma points and propagated them through the original nonlinear system. Simulation results illustrated superior performance of UKF for vehicle inertial parameter identifcation. Hashemi *et al.* [14] proposed a new Kalman-based observer to address measurement uncertainties. This was achieved by considering tire nonlinearities with a minimum number of required tire parameters and road condition as uncertainty. Longitudinal forces obtained by UKF for wheel dynamics is employed as an observation for Kalman-based velocity estimator at each corner. Results showed higher accuracy and robustness of the proposed approach in estimating longitudinal speed for ground vehicles. Liu *et al.* [15] proposed a novel Adaptive Unscented Kalman filter (AUKF) based on three data-fusing approaches to estimate system state. Experiments demonstrated that AUKF reduced state estimation error by approximately 65% to improve performance robustness. Hong *et al.* [16] used a dual UKF to identify inertial parameters and vehicle state. Simulations and experimental results demonstrated robustness of the proposed approach on a flat road with a constant tire–road friction coefficient.

In the methods presented above, process noise variance Q and measurement noise covariance matrix $\boldsymbol{R}$ were selected through empirical data or assumed to be constant, i.e. variations of the road were not taken into account. This is contrary to real situations, where Q and $\boldsymbol{R}$ are variants and under practical conditions, roads are complex and uncertain. The main contribution of this paper lies in the consideration of process noise variance and measurement noise covariance of various road conditions and its corresponding relationship. Additionally, a probabilistic neural network (PNN) classifier is used to estimate road excitation level.

To deal with the above mentioned problems, the following two aspects are taken into account:

- Relationship between Q and $\boldsymbol{R}$ variations on UKF performance from observer perspective are comprehensively analyzed;
- Concept of road estimation based AUKF is proposed and its performance is compared to UKF under varying driving conditions.

In this paper, influence of Q and $\boldsymbol{R}$ on estimation accuracy of UKF is first analyzed. Also, imperative of road process noise on estimation of suspension state is illustrated. Then, an effective road classification method is introduced by combining time and frequency domain information from sprung and unsprung mass acceleration signals. Classification accuracy of varied working conditions is compared. Simulation results show that the proposed method can improve estimation accuracy compared to UKF. Based on the full-car nonlinear model and road classification approach, Q and $\boldsymbol{R}$ are tuned and are used to form the AUKF algorithm for improving overall performance from observer perspective.

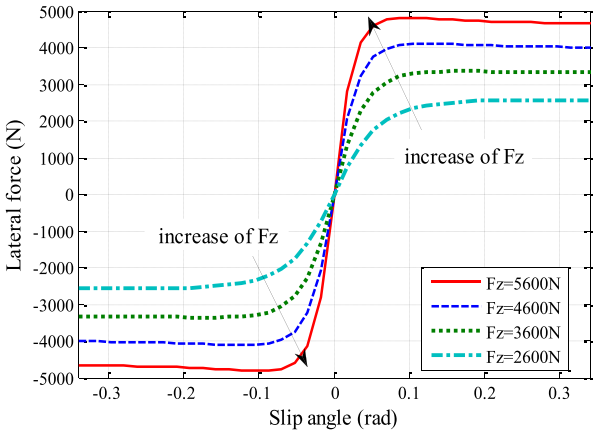

FIGURE 1. Influence of vertical force on tire lateral force.

The rest of the paper is organized as follows. In Section II, a full-car nonlinear model and road classification method are studied. In Section III, a flow chart of the AUKF algorithm is proposed to estimate state of vehicle system. In Section IV, analysis of the vehicle system based on road classification is performed using the AUKF method. Simulation results show that the proposed AUKF method is more effective compared with existing UKF approach. Additionally, the method demonstrates importance of considering road level information in the process of state estimation of a vehicle system. Finally, conclusions are discussed in Section V.

II. SYSTEM MODEL

A. TIRE MODELING

The Magic Formula (MF) Tire Model established by Pacejka [17] is utilized here. MF is a commonly used tire model which has a general form as shown below:

$$y = D\sin[C\arctan\{Bx - E(Bx - \arctan(Bx))\}] \quad (1)$$

$$Y(X) = y(x) + S_{\mathrm{V}}$$
$$x = X + S_{\mathrm{H}} \quad (2)$$

where X is input state, which represents slip ratio or slip angle; Y is output state and represents longitudinal force, lateral force or aligning torque. Factors C, D, B and E are usually derived from experiments. D is peak value of the curve; Cdetermines shape of the obtained curve; B represents stiffness value of the curve; E represents curvature of the curve; S_{H} and S_{v} are offset values of input and output states.

For the known MF model, performance of tire models for the vehicle can be acquired as shown in Fig. 1.

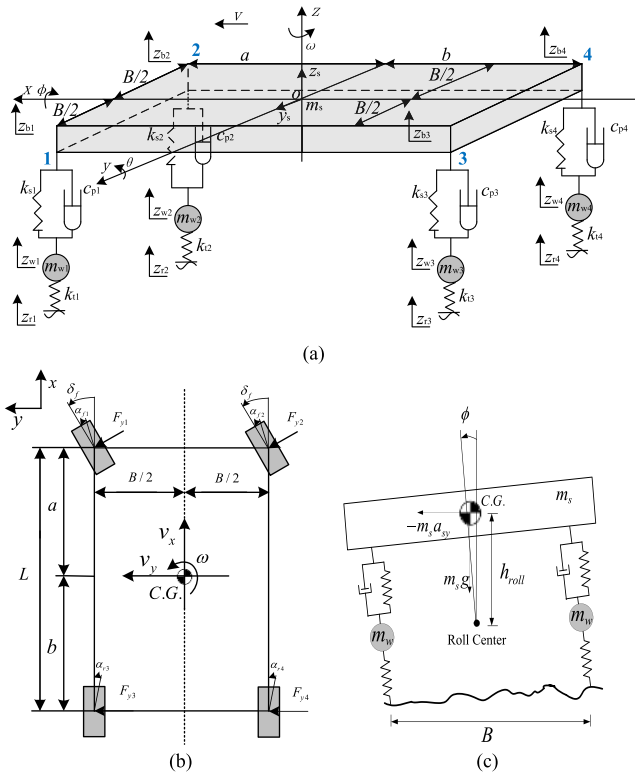

FIGURE 2. 9-DOF vehicle dynamics model. (a) Full-car dynamics model (b) Lateral dynamics model (c) Roll dynamics model.

B. FULL-CAR DYNAMICS MODEL

In this section, a nonlinear vehicle model with road excitation taken into consideration is presented. Various vehicle models have been proposed to study vehicle dynamics [18], [19]. Due to the complexity and uncertainty associated with practical vehicle driving and road conditions, front and rear coherence properties of a vehicle and the road can not be ignored. A comprehensive and practical model of a nine degree of freedom (9-DOF) full car is presented in this paper. Schematic of a full car system with passive suspension is shown in Fig. 2. This model includes 3-DOF for pitch, vertical, and roll movement of the vehicle, 4-DOF for vertical movement of unsprung masses, and 2-DOF for vehicle lateral and yaw movement. Symbols used in Fig. 2 are listed in Table 1. Parameters in Table 1 are from CarSim® (C-Class, Hatchback).

The 9-DOF dynamics model is developed based on the following assumptions [17], [20].

1) There is no slip between the tires and road surface, and influence of longitudinal force of the tires was not considered.
2) Effect of air force was ignored.
3) Suspension deformation steering and change in steering wheel alignment parameters were ignored.

Based on Newton's law, dynamics equations for a 9-DOF full car model are as follow.

TABLE 1. Description of symbols used for 9-DOF full-car dynamics model.

Vehicle model parameters	Symbol	Unit	Value	Remark
Distance from C.G. to front axle	a	m	1.18	Measurement
Distance from C.G. to rear axle	b	m	1.77	Measurement
Lateral acceleration	a_y	m/s^2	-	Calculation
Rear tire slip angle	α_r	deg(°)	--	Calculation
Suspension stiffness of left front side	k_{s1}	N/m	14000	Measurement
Suspension stiffness of right front side	k_{s2}	N/m	14000	Measurement
Suspension stiffness of left rear side	k_{s3}	N/m	14000	Measurement
Suspension stiffness of right rear side	k_{s4}	N/m	14000	Measurement
Suspension damping coefficient of left front side	c_{p1}	Ns/m	1500	Measurement
Suspension damping coefficient of right front side	c_{p2}	Ns/m	1500	Measurement
Suspension damping coefficient of left rear side	c_{p3}	Ns/m	1500	Measurement
Suspension damping coefficient of right rear side	c_{p4}	Ns/m	1500	Measurement
Tire stiffness of left front side	k_{t1}	N/m	230000	Measurement
Tire stiffness of right front side	k_{t2}	N/m	230000	Measurement
Tire stiffness of left rear side	k_{t3}	N/m	230000	Measurement
Tire stiffness of right rear side	k_{t4}	N/m	230000	Measurement
Unsprung mass of left front side	m_{w1}	k_g	60	Measurement
Unsprung mass of right front side	m_{w2}	k_g	60	Measurement
Unsprung mass of left rear side	m_{w3}	k_g	60	Measurement
Unsprung mass of right rear side	m_{w4}	k_g	60	Measurement
Sprung mass displacement	z_b	m	--	Measurement
Road profile of left front side	z_{r1}	m	--	Calculation
Road profile of right front side	z_{r2}	m	--	Calculation
Road profile of left rear side	z_{r3}	m	--	Calculation
Road profile of right rear side	z_{r4}	m	--	Calculation
Distance between roll center to C.G. of sprung mass	h_{roll}	m	0.9	Measurement
Roll angle	φ	deg (°)	--	Calculation
Pitch angle	θ	deg (°)	--	Calculation

a) Equation (3) expresses vehicle body vertical motion

$$\sum_{i=1}^{4} F_{si} = -m_s \ddot{z}_s \tag{3}$$

where F_{si} is suspension force. Corresponding equations can be obtained as follows.

$$F_{s1} = -k_{s1}(z_{b1} - z_{w1}) - c_{p1}(\dot{z}_{b1} - \dot{z}_{w1});$$

$$
\begin{aligned}
F_{s2} &= -k_{s2}(z_{b2} - z_{w2}) - c_{p2}(\dot{z}_{b2} - \dot{z}_{w2});\\
F_{s3} &= -k_{s3}(z_{b3} - z_{w3}) - c_{p3}(\dot{z}_{b3} - \dot{z}_{w3});\\
F_{s4} &= -k_{s4}(z_{b4} - z_{w4}) - c_{p4}(\dot{z}_{b4} - \dot{z}_{w4});
\end{aligned} \tag{4}
$$

and,

$$
\begin{aligned}
z_{b1} &= z_b + \frac{B}{2}\sin\phi - a\sin\theta;\\
z_{b2} &= z_b - \frac{B}{2}\sin\phi - a\sin\theta;\\
z_{b3} &= z_b + \frac{B}{2}\sin\phi + b\sin\theta;\\
z_{b4} &= z_b - \frac{B}{2}\sin\phi + b\sin\theta;
\end{aligned} \tag{5}
$$

b) Equation (6) is for unsprung mass vertical motion

$$
\begin{aligned}
m_{w1}\ddot{z}_{w1} &= -k_{s1}(z_{w1} - z_{b1}) - c_{p1}(\dot{z}_{w1} - \dot{z}_{b1})\\
&\quad - k_{t1}(z_{w1} - z_{r1});\\
m_{w2}\ddot{z}_{w2} &= -k_{s2}(z_{w2} - z_{b2}) - c_{p2}(\dot{z}_{w2} - \dot{z}_{b2})\\
&\quad - k_{t2}(z_{w2} - z_{r2});\\
m_{w3}\ddot{z}_{w3} &= -k_{s3}(z_{w3} - z_{b3}) - c_{p3}(\dot{z}_{w3} - \dot{z}_{b3})\\
&\quad - k_{t3}(z_{w3} - z_{r3});\\
m_{w4}\ddot{z}_{w4} &= -k_{s4}(z_{w4} - z_{b4}) - c_{p4}(\dot{z}_{w4} - \dot{z}_{b4})\\
&\quad - k_{t4}(z_{w4} - z_{r4});
\end{aligned} \tag{6}
$$

where M_{xi}, $i = 1, 2, 3, 4$ is vehicle roll moment.

c) Equation (7) is for vehicle body pitch motion

$$
\begin{aligned}
\sum_{i=1}^{4} M_{yi} = I_{yi}\ddot{\theta} &= (F_{s1} + F_{s2})a - (F_{s3} + F_{s4})b\\
&\quad + m_s g h_{roll}\sin\theta
\end{aligned} \tag{7}
$$

where M_{yi}, $i = 1, 2, 3, 4$ is vehicle roll moment.

d) Equation (8) expresses vehicle body roll motion

$$
\begin{aligned}
\sum_{i=1}^{4} M_{xi} = I_x\ddot{\phi} &= (F_{s2} + F_{s4})\frac{B}{2} - (F_{s1} + F_{s3})\frac{B}{2}\\
&\quad + m_s h_{roll}(g\sin\theta + a_{sy})
\end{aligned} \tag{8}
$$

where M_{zi}, $i = 1, 2, 3, 4$ is tire self-aligning moment.

e) Equation (9) expresses vehicle lateral motion

$$
\begin{aligned}
\sum_{i=1}^{4} F_{yi} &= \sum_{i=1}^{4} m_{wi}a_{wyi}\\
&= (F_{y1} + F_{y2})\cos\delta_f + (F_{y3} + F_{y4})\cos\delta_r;
\end{aligned} \tag{9}
$$

where F_{yi}, $i = 1, 2, 3, 4$, is tire lateral force.

f) Equation (10) is for vehicle yaw motion

$$
\begin{aligned}
\sum_{i=1}^{4} M_{zi} = I_z\dot{\omega} &= b(F_{y3} + F_{y4})\cos\delta_r - a(F_{y1} + F_{y2})\\
&\quad \times \cos\delta_f - B/2(F_{y2} - F_{y1})\sin\delta_r\\
&\quad - B/2(F_{y4} + F_{y3})\sin\delta_f
\end{aligned} \tag{10}
$$

If we assume vehicle system state and measurement output vectors are chosen as:

$$
\begin{aligned}
\mathbf{x} &= [\dot{x}_b, \dot{\theta}, \dot{\phi}, x_{b1} - x_{w1}, x_{b2} - x_{w2}, x_{b3} - x_{w3}, x_{b4} - x_{w4},\\
&\quad \dot{x}_{w1}, \dot{x}_{w2}, \dot{x}_{w3}, \dot{x}_{w4}, x_{w1} - x_{r1}, x_{w2} - x_{r2}, x_{w3} - x_{r3},\\
&\quad x_{w4} - x_{r4}]^T;\\
\mathbf{y} &= [\ddot{x}_b, \dot{\theta}, \dot{\phi}, \ddot{x}_{w1}, \ddot{x}_{w2}, \ddot{x}_{w3}, \ddot{x}_{w4}]^T;
\end{aligned} \tag{11}
$$

where fifteen states are velocity of vehicle body sprung mass, pitch angle rate, roll angle rate, rattle space of left front side, rattle space of right front side, rattle space of left rear side, rattle space of right rear side, unsprung mass velocity of left front side, unsprung mass velocity of right front side, unsprung mass velocity of left rear side, unsprung mass velocity of right rear side, tire deflection of left front side, tire deflection of right front side, tire deflection of left rear side and tire deflection of right rear side, respectively. Outputs are acceleration of vehicle body sprung mass, pitch angle rate, roll angle rate, unsprung mass acceleration of left front side, unsprung mass acceleration of right front side, unsprung mass acceleration of left rear side and unsprung mass acceleration of right rear side.

Thus, state space equation can be further expressed as follows.

$$\dot{\mathbf{x}} = \mathbf{A}\mathbf{x} + \mathbf{B}\mathbf{u} + \mathbf{\Gamma}w \tag{12}$$

$$\mathbf{y} = \mathbf{C}\mathbf{x} + \mathbf{D}\mathbf{u} + \mathbf{v} \tag{13}$$

where, $\mathbf{A}$, $\mathbf{B}$, $\mathbf{\Gamma}$, $\mathbf{C}$ and $\mathbf{D}$ are described in Appendix A; w and $\mathbf{v}$ are vehicle system process and measurement noise, respectively, which are assumed to be independent and Gaussian.

Discrete-time formulation of the state-space representation can be expressed using Equation (14) and Equation (15) [5], [21], [22]:

$$\mathbf{x}_{k+1} = \mathbf{\Phi}\mathbf{x}_k + \mathbf{E}\mathbf{u}_k + \mathbf{\Gamma}'w_k \tag{14}$$

$$\mathbf{y}_k = \mathbf{H}\mathbf{x}_k + \mathbf{I}\mathbf{u}_k + \mathbf{v}_k \tag{15}$$

Then, k denotes the discrete-time instant k T, with T as time step. In Equation (14) and Equation (15), $\mathbf{\Phi}$ is a 15×15 system transition matrix, $\mathbf{x}$ is a 15×1 state vector, $\mathbf{E}$ is a 15×4 state vector, $\mathbf{u}$ is a 4×1 state vector, $\mathbf{\Gamma}'$ is a 15×4 constant input matrix, $\mathbf{y}_i$ is a 7×1 measurement vector, and $\mathbf{H}$ is a 7×15 output matrix. w_k (4×1) and $\boldsymbol{\nu}_k(7 \times 1)$ represent uncorrelated Gaussian white noise sequences, with $Q = E(w_k w_k^T)$ and $\boldsymbol{R} = E(v_k v_k^T)$ being their corresponding process noise variance and measurement noise covariance matrices, respectively. Q and $\boldsymbol{R}$ are bounded positive definite matrices (i.e. $Q > 0$, $\boldsymbol{R} > 0$) [23], [24].

The vehicle system is assumed to be completely observable and controllable, i.e.

$$
\begin{aligned}
rank[\mathbf{H}^T, (\mathbf{H}\mathbf{\Phi})^T, (\mathbf{H}\mathbf{\Phi}^\mathbf{2})^T, (\mathbf{H}\mathbf{\Phi}^\mathbf{3})^T] &= 15\\
rank[\mathbf{\Gamma}', \mathbf{\Phi}\mathbf{\Gamma}', \mathbf{\Phi}^\mathbf{2}\mathbf{\Gamma}', \mathbf{\Phi}^\mathbf{3}\mathbf{\Gamma}'] &= 15
\end{aligned} \tag{16}
$$

C. LATERAL ACCELERATION

Write instead, "The potential was calculated by using (1)," or "Using (1), we calculated the potential."

As shown in Fig. 2(b), dynamics equations of the full-car model can be expressed as follows:

$$\begin{aligned} ma_y - m_s h_s \ddot{\phi} - \left(F_{yf} + F_{yr}\right) &= 0 \\ I_z \dot{\gamma} + I_{zx} \ddot{\phi} - I_{xy} \ddot{\phi}^2 - \left(aF_{yf} - bF_{yr} + M\right) &= 0 \end{aligned} \quad (17)$$

where I_z, I_{xy} and I_{zx} are moment of inertia along Z axis, X-Y axis and Z-X axis, respectively. M is steering moment.

To solve for desired lateral acceleration, according to vehicle theory [19], slip angles can be calculated as follows:

$$\begin{cases} \alpha_f = \dfrac{v_y}{v_x} + \dfrac{a\gamma}{v_x} - \delta_f \\ \alpha_r = \dfrac{v_y}{v_x} - \dfrac{b\gamma}{v_x} \end{cases} \quad (18)$$

Acceleration in Y-direction and yaw angle are obtained as follows:

$$\begin{aligned} \dot{v}_y = &\frac{-2\left(C_f + C_r\right) v_y - 2\left(aC_f - bC_r\right)\gamma}{M_1 \cdot v_x} \\ &+ \frac{2C_f \cdot \delta_f}{M_1} - v_x \cdot \gamma \end{aligned} \quad (19)$$

$$\begin{aligned} \dot{\gamma} = &\frac{-2\left(aC_f - bC_r\right) v_y - 2\left(a^2 C_f + b^2 C_r\right)\gamma}{I_z \cdot v_x} \\ &+ \frac{2a \cdot C_f \cdot \delta_f}{I_z} \end{aligned} \quad (20)$$

Desired lateral acceleration for a driver's steering input is expressed as follows:

$$\begin{aligned} a_y = \dot{v}_y + v_x \gamma = &\frac{-2\left(C_f + C_r\right) v_y - 2\left(aC_f - bC_r\right)\gamma}{M_1 \cdot v_x} \\ &+ \frac{2C_f \cdot \delta_f}{M_1} \end{aligned} \quad (21)$$

Remark: Tire cornering stiffness is calculated using MF in section II, and other parameters can be obtained using CarSim® simulation.

D. ROAD CLASSIFICATION

Qin *et al.* [23] proposed an novel approach to classify road excitations based on measurable suspension system response (i.e. vertical acceleration of sprung mass and unsprung mass). In this paper, response signal was first decomposed by wavelet packet analysis. Next, features in both time and frequency domains were extracted. Then, minimum redundancy maximum relevance (mRMR) was utilized to select superior features. A Probabilistic Neural Network (PNN) classifier was applied to these selected features to determine road classification output. Fig. 3 shows the process of the proposed method and details are explained in [23].

According to [23], merits of the proposed classification method can be summarized as follows:

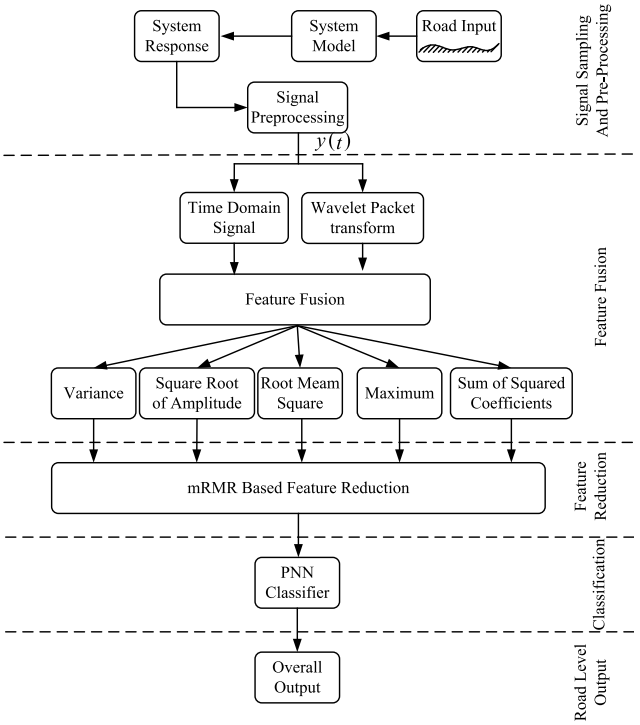

FIGURE 3. Proposed of road classification method.

(1) Higher estimation accuracy. Classification accuracy and robustness of the proposed method are compared to existing methods with varying driving conditions;
(2) More practical applications. The proposed method can accurately estimate varying road excitation with different frequency structure, which makes it more suitable for practical applications;
(3) More information used. Combing information available from both time and frequency domain, and the features in different frequency ranges are fully investigated and utilized develops this method.

III. VEHICLE SYSTEM STATE ESTIMATION USING THE AUKF ALGORITHM

Road classification and UKF are combined to form AUKF. A chart illustrating this process is shown in Fig. 4. Next, for application of UKF, Q and $\boldsymbol{R}$ need to be defined using a priori information about perturbation w_k acting on the state Equation (14), and $\boldsymbol{v}_k$ acting on the measurement Equation (15). The tuning operation constitutes a critical step to sure accuracy of the estimation algorithm. Value of the Q and $\boldsymbol{R}$ may be acquired from modeling errors. More precisely, it is likely that these errors occur during comparison between the reference state and predicted dynamic evolution of the state vector, and w_k may be utilized to account for these errors. Also, relation linking measured output vector $\boldsymbol{v}_k$ and state vector depends on measurement equipment and the chosen model [24]. The process of tuning state vector values for application of the

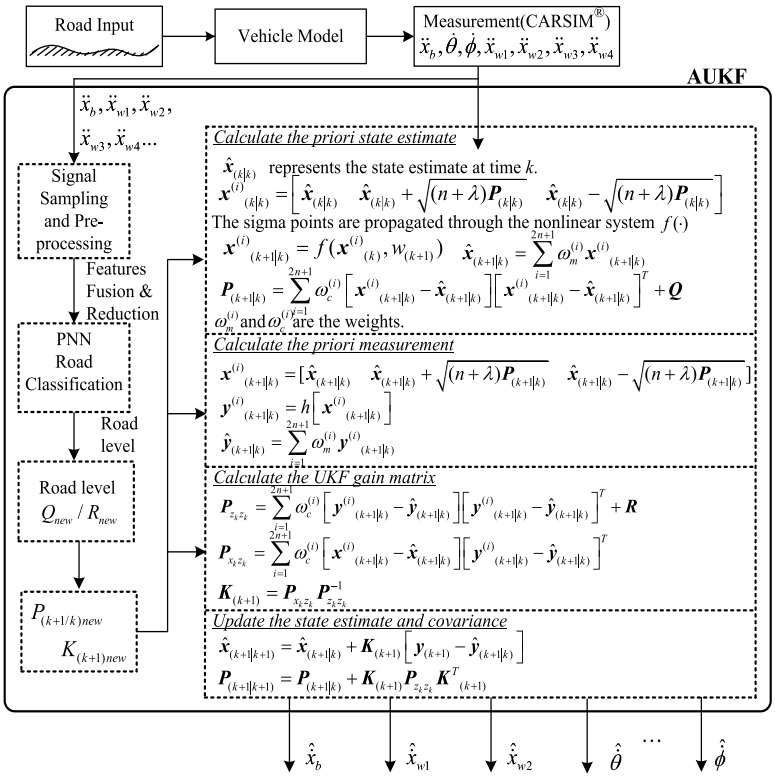

FIGURE 4. Flow chart of AUKF algorithm for vehicle system state estimation.

AUKF under various road excitations is further elaborated in the following section.

A. ESTIMATION OF ROAD PROCESS NOISE VARIANCE Q

To solve for optimal results with UKF, system noise should be Gaussian white noise [5], [21]. Using road level definition proposed in Section 2.3, power spectral density (PSD) of uneven road under different road excitation levels could be obtained. According to [25], relationship between PSD of road roughness and PSD of road velocity can be expressed as:

$$G_{\dot{q}}(n) = (2\pi n)^2 G_q(n) \tag{22}$$

Equation (22) combined with International Standards Organization (ISO) 8601 [26], i.e. $w = 2$, can be used to obtain:

$$G_{\dot{q}}(n) = (2\pi n_0)^2 G_q(n_0) \tag{23}$$

Here, $G_{\dot{q}}(n)$ includes for the entire frequency spectrum with (the upper and lower spatial frequencies set as $0.011m^{-1}$ and $2.83m^{-1}$ [26]. In this case, velocity of the road uneven is white noise. Variance of different road levels ($A \sim H$) can be calculated using the above analysis. Assuming that velocity of the vehicle is 80km/h, PSD of road velocity relationship for temporal frequency of different road levels is as shown in Fig. 5. Corresponding road velocity process noise variance Q is acquired using product of the area of temporal frequency

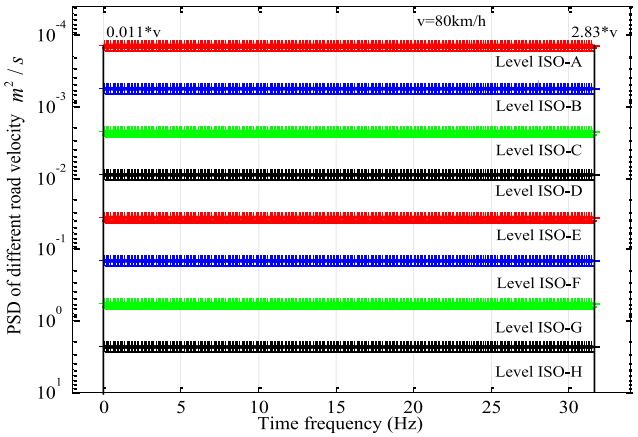

FIGURE 5. PSD of different road velocities under different temporal frequency range.

range and different road velocities PSD values for certain frequencies, as listed in Table 2.

It can be seen from results in Table 2 that value of Q increased for higher road levels, increasing by a factor of approximately 4 for each increase in road level [24].

B. ESTIMATION OF MEASUREMENT NOISE COVARIANCE R

Value of $\boldsymbol{R}$ for application of UKF is assumed to be constant and is determined through empirical assessment [10]–[14].

TABLE 2. Road level process noise variance Q.

Road Level	Process Noise Variance Q (m/s2)	Road Level	Process Noise Variance Q (m/s2)
A	0.0022	E	0.5624
B	0.0088	F	2.2495
C	0.0351	G	8.9979
D	0.1406	H	35.992

However, road information is complex and uncertain in practical settings. The covariance $\boldsymbol{R}$ is dependent on sensor output and road conditions. To improve accuracy in the estimation of $\boldsymbol{R}$, an approach has been proposed in [24] and [27] and adopted in this paper. Based on this method, $\boldsymbol{R}$ can be calculated as.

$$\mathbf{R} = \mathbf{HPH}^T - \mathbf{C}_n \tag{24}$$

where, $\mathbf{C}_n$ and $\mathbf{PH}^T$ are defined as follows:

$$\begin{aligned}
\mathbf{C}_1 &= \mathbf{H\Phi PH}^T - \mathbf{H\Phi KC}_0 \\
\mathbf{C}_2 &= \mathbf{H\Phi}^2\mathbf{PH}^T - \mathbf{H\Phi KC}_1 - \mathbf{H\Phi}^2\mathbf{KC}_0 \\
\mathbf{C}_3 &= \mathbf{H\Phi}^3\mathbf{PH}^T - \mathbf{H\Phi KC}_2 - \mathbf{H\Phi}^2\mathbf{KC}_1 - \mathbf{H\Phi}^3\mathbf{KC}_0 \\
&\vdots \\
\mathbf{C}_n &= \mathbf{H\Phi}^n\mathbf{PH}^T - \mathbf{H\Phi KC}_{n-1} - \cdots - \mathbf{H\Phi}^n\mathbf{KC}_0;
\end{aligned}$$

$$\mathbf{PH}^T = \begin{bmatrix} \mathbf{H} \\ \mathbf{H\Phi} \\ \vdots \\ \mathbf{H\Phi}^{n-1} \end{bmatrix}^* \times \begin{bmatrix} \mathbf{C}_1 + \mathbf{H\Phi}K\mathbf{C}_0 \\ \mathbf{C}_2 + \mathbf{H\Phi}K\mathbf{C}_1 + \mathbf{H\Phi}^2K\mathbf{C}_0 \\ \vdots \\ \mathbf{C}_n + \mathbf{H\Phi}K\mathbf{C}_{n-1} + \cdots + \mathbf{H\Phi}^nK\mathbf{C}_0 \end{bmatrix};$$

where $\mathbf{H}$ represents system output matrix, $\mathbf{C}_0$ is initial measurement noise covariance, $\mathbf{P}$ represents covariance equations of KF, $\mathbf{\Phi}$ is system transition matrix, and $\mathbf{K}$ represents KF gain. The more details are described in [24] and [27].

Measurement noise covariance matrix $\boldsymbol{R}$ should be updated with process noise covariance matrix Q. More information are described in [28]. Based on the above analysis and considering measurement noise covariance values of sprung mass and unsprung mass, values of $\boldsymbol{R}$ for different road levels ($A \sim H$) were calculated. Results are listed in Table 3. Table 3 shows that value of $\boldsymbol{R}$ increased for higher road levels, but less so than Q.

C. AUKF FILTERING BASED ON NOISE Q AND R ESTIMATION

Based on analysis describe in Sections *A* and *B*, traditional UKF can be reduced by combining discrete-time state Equation (14) and Equation (15) for each state. The reduce UKF

TABLE 3. Road level measurement noise covariance matrix R.

Road Level	Accelerator Measurement Noise Covariance $\boldsymbol{R}$	Road Level	Accelerator Measurement Noise Covariance $\boldsymbol{R}$
A	0.165e-5*I	E	4.224e-4*I
B	0.66e-5*I	F	1.689e-3*I
C	2.64e-5*I	G	6.758e-3*I
D	1.056e-4*I	H	2.703e-2*I

Note: **I** is unit matrix.

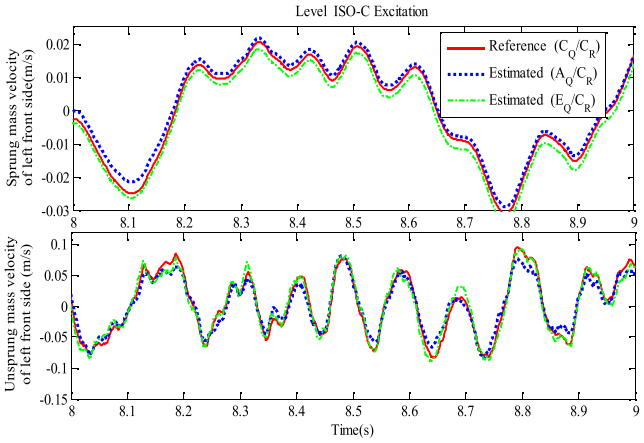

FIGURE 6. Effect of road level ISO-A/E process variance Q on road level ISO-C measurement covariance R.

expression is given as [16], [29]:

$$\begin{aligned}
\chi_0 &= \bar{x}; \quad \chi_i = \bar{x} + (\sqrt{(n+\lambda)\,\mathbf{P}})_i; \quad i = 1, 2, \cdots n; \\
\chi_i &= \bar{x} - (\sqrt{(n+\lambda)\,\mathbf{P}})_i; \quad i = 1, 2, \cdots n; \\
\varpi_m^0 &= \frac{\lambda}{n+\lambda}; \quad \varpi_c^0 = \frac{\lambda}{n+\lambda} + 1 - \alpha^2 + \beta; \\
\varpi_m^i &= \varpi_c^i = \frac{1}{2}(n+\lambda);
\end{aligned} \tag{25}$$

where $\lambda = \alpha^2(n+\kappa) - p$ is a scaling parameter, α is set to a small positive value, κ represents a secondary scaling parameter, and β is utilized to incorporate a priori information of the distribution of $\mathbf{x}$. $\sqrt{(n+\lambda)}\mathbf{P}_x$ represents the ith row of the matrix square root.

$$\begin{aligned}
\hat{x}_{k+1}^- &= \sum_{i=0}^{2n} \varpi_i^m \chi_{k|k-1}; \\
p_k^- &= \sum_{i=0}^{2n} \varpi_m^i (\chi_{i,k|k-1} - \hat{x}_k^-)(\chi_{i,k|k-1} - \hat{x}_k^-)^T + Q_k; \\
P_{zk} &= \sum_{i=0}^{2n} \varpi_c^i \{y_i - \bar{y}\}\{y_i - \bar{y}\}^T + R_k; \quad \bar{y} = \sum_{i=0}^{2n} \varpi_m^i y_i; \\
P_{xkzk} &= \sum_{i=0}^{2n} \varpi_c^i (\chi_{i,k|k-1} - \hat{y}_k^-)(\chi_{i,k|k-1} - \hat{y}_k^-)^T; \\
K_k &= P_{xkzk} P_{xkzk}^{-1}; \quad \hat{x}_k = x_k + K_k(y_k - \hat{y}_k^-); \\
P_k &= P_k^- - K_k P_{zk} K_k^T
\end{aligned} \tag{26}$$

TABLE 4. Error value of sprung mass and unsprung mass velocity based on above simulations.

Estimation Error	Estimation Parameters (m/s^2)	Road level ISO-*A* Covariance ***R*** for Road level ISO-*C* Excitation	Road level ISO-*A* Variance Q for Road level ISO-*C* Excitation	Road level ISO-*E* Covariance ***R*** for Road level ISO-*C* Excitation	Road level ISO-*E* Variance Q for Road level ISO-*C* Excitation
Root mean square(RMS)	$\dot{x}_b$	0.009	0.039	0.16	0.019
	$\dot{x}_{wl}$	0.039	0.179	1.021	0.099

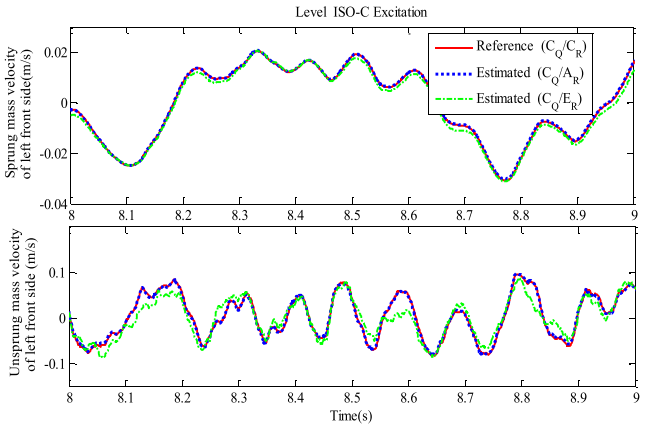

FIGURE 7. Effect of road level ISO-*A*/*E* measurement covariance ***R*** on road level ISO-*C* process variance ***Q***.

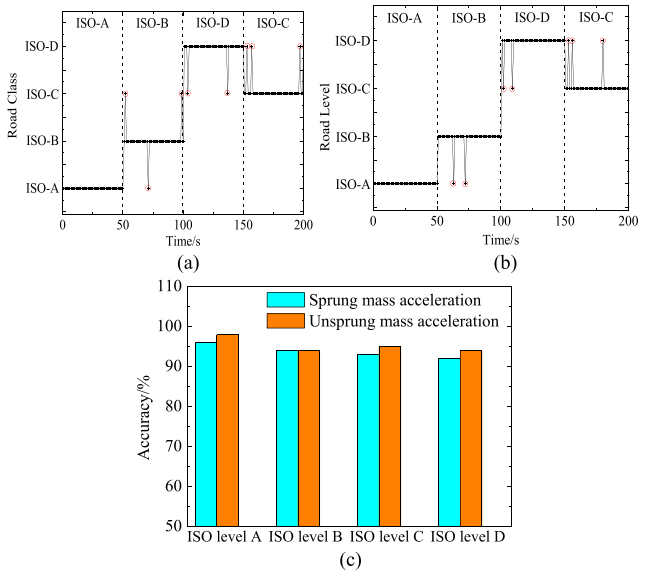

FIGURE 8. Classification results for different road levels: a) sprung mass acceleration; b) unsprung mass acceleration; c) road level classification accuracy.

where, P_k represents estimation error variance matrix, K_k is Kalman gain. Note that Q and ***R*** are assumed to be tuned. A detailed flow chart illustrating the steps involved in AUKF is shown in Figure 4. Process noise variance Q and measurement noise covariance matrix ***R*** of different road levels are obtained using methods describe in Sections *A* and *B*.

IV. SIMULATIONS AND RESULTS

A. EFFECT OF Q/R ON ESTIMATION ACCURACY

In this section, vehicle system is subjected to road level ISO-*C* excitation. This excitation allows influence of ***R*** and Q values on vehicle state observation accuracy to be studied. Values of Q and ***R*** are set for level ISO-*A* and ISO-*E*, respectively, with a vehicle velocity of 40km/h to illustrate influence of mismatched noise. Vehicle observation was simulated in MATLAB, and sprung mass and unsprung mass velocities of the left front side were taken as estimated states. Generally speaking, influence of noise needs to be eliminated with the magnitude as low as possible, while original signal information needs to be maintained [27]. Simulations were carried out for a run time of 15 seconds to obtain filter results. To illustrate the results from the following simulation situations, we first defined a feature set with different road and noise variance values, i.e. $\Theta_{\Im}$, where $\Theta \in \{A, B, \cdots G\}$ is different road level set, $\Im \in \{Q, \mathbf{R}\}$ for process variance and noise covariance of Θ.

To facilitate ease of comparisons, simulation results from time segment ranging from of 8 to 9 seconds are shown in Figs. 6 and 7. It can be seen from the results listed in Table 4 that value of ***R*** has more influence on reference results compared to Q. The statistics of the estimation error and noise variance are relevant, and the results are also shown in Table 4. Fig.6 shows that when ***R*** is constant, increased influence on results was observed for increased values of Q. Conversely, Fig.7 shows that when Q is kept constant, an increased influence was observed for decrease in ***R***.

Table 4 shows a significant difference between RMS error value of Q and **R** with road level ISO-*A* or ISO-*E* under the level ISO-*C* excitation, i.e. velocity error of vehicle unsprung mass RMS value is larger than sprung mass velocity error, and value of **R** has greater influence than Q.

Based on the above analysis, it was observed that error estimation of road information leads to error estimation of Q or***R***, thus affecting results of UKF in this situation and vice versa. So, it is necessary that appropriate value of the noise variance matrix is chosen under various conditions [24].

B. EFFECT OF Q/R ON ESTIMATION ACCURACY

To validate the proposed approach in Section II, a novel road profile was generated. The road profile was composed of four road levels: level ISO-*A*, level ISO-*B*, level ISO-*C* and level ISO-*D*, in succession [30]. Simulation results obtained

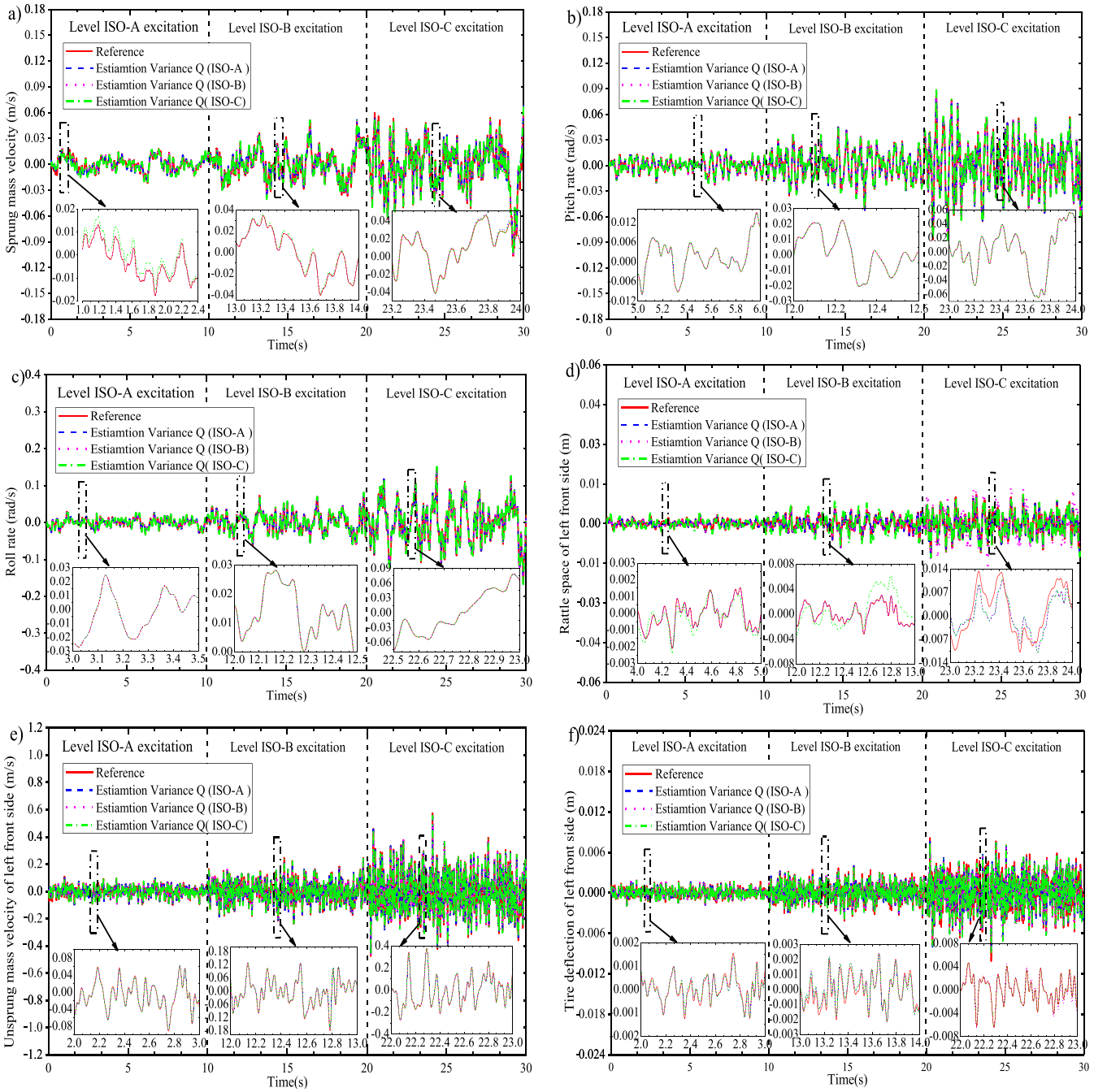

FIGURE 9. Estimation results of road level ISO-*A*/*B*/*C* excitation and using level ISO-*A*/*B*/*C* process variance *Q*. (a) Sprung mass velocity (b) Pitch rate (c) Roll rate (d) Rattle space of left front side (e) Unsprung mass velocity of left front side (f) Tire deflection of left front side.

with system parameters and conditions defined are obtained in [25] and shown in Fig. 8.

As seen in Fig. 8, two system responses can accurately identify all four road levels with accuracy of more than 85%. Both sprung mass and unsprung mass acceleration demonstrated improved performance. Lowest classification accuracy of these two responses was 94%. It can also be observed from Figs. 8 (a) and (b) that almost all classification errors occur when road level changes. Although, transformation time is significantly short between different road levels, such kind of aliasing is unavoidable. In addition, error points shown in Figs. 8 (a) and (b) indicate difference of two adjacent roads would also significantly influence classification accuracy. When difference was relatively large, errors were observed, which were related to the difference.

C. AUKF ALGORITHM SIMULATIONS AND RESULTS

The AUKF method proposed in Section III allows state of vehicle system to be estimated. In this case, system definition

TABLE 5. Estimation accuracy of different road excitation levels using different road process noise variance *Q*.

--	Road level ISO-*A* Excitation				Road level ISO-*B* Excitation				Road level ISO-*C* Excitation			
	Accuracy of state estimation / %											
	$\dot{x}_b$	$x_{b1}-x_{w1}$	$\dot{x}_{w1}$	$x_{w1}-x_{r1}$	$\dot{x}_b$	$x_{b1}-x_{w1}$	$\dot{x}_{w1}$	$x_{w1}-x_{r1}$	$\dot{x}_b$	$x_{b1}-x_{w1}$	$\dot{x}_{w1}$	$x_{w1}-x_{r1}$
Variance	***R*** with Road Level ISO-*A*				***R*** with Road Level ISO-*B*				***R*** with Road Level ISO-*C*			
Q with Road Level ISO-*A*	**96.2**	**92.5**	**96.2**	**96.3**	93.5	79.4	87.9	87.4	72.5	82.4	84.5	80.5
Q with Road Level ISO-*B*	95.1	88.4	87.6	94.2	**97.4**	**90.6**	**97.9**	**95.3**	85.9	87.1	88.6	84.3
Q with Road Level ISO-*C*	94.5	82.5	83.2	92.4	86.3	83.0	83.6	79.7	**97.1**	**93.7**	**95.8**	**94.3**

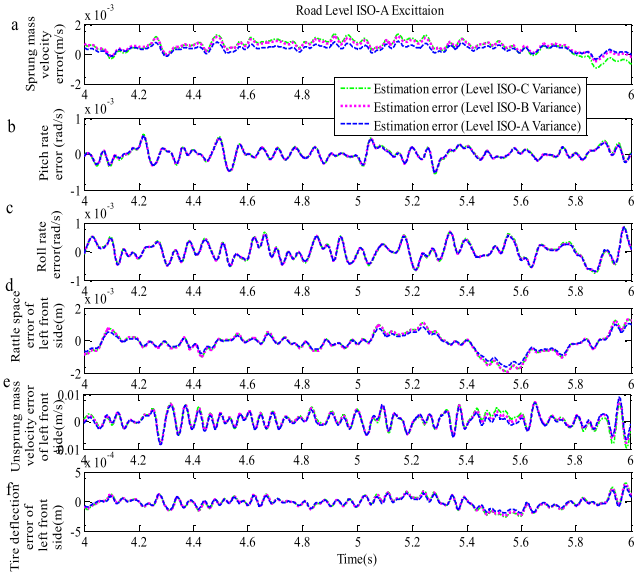

FIGURE 10. Error of state estimation for road level ISO-*A* excitation using level ISO-*A*/*B*/*C* process variance *Q* (a) Sprung mass velocity of vehicle body (b) Pitch rate (c) Roll rate (d) Rattle space of left front side (e) Unsprung mass velocity of left front side (f) Tire defection of left front side.

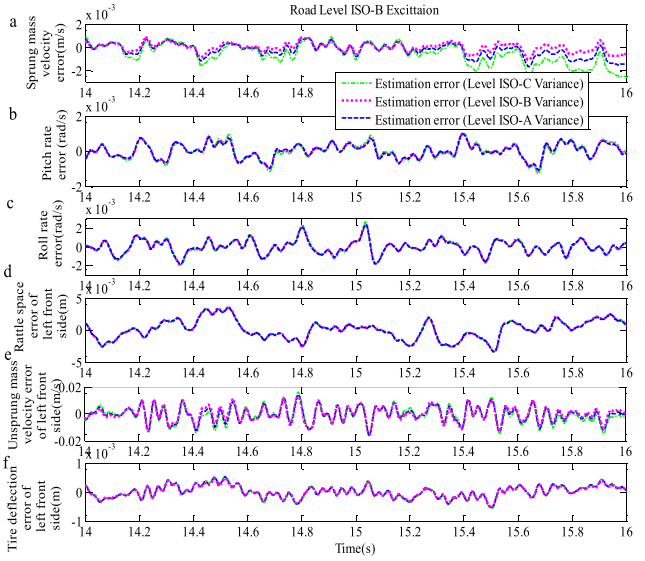

FIGURE 11. Error of state estimation for road level ISO-*B* excitation using level ISO-*A*/*B*/*C* process variance *Q* (a) Sprung mass velocity of vehicle body (b) Pitch rate (c) Roll rate (d) Rattle space of left front side (e) Unsprung mass velocity of left front side (f) Tire defection of left front side.

listed Table 1 was adopted, and initial velocity was set to 40km/h. Due to tire hop, errors in state estimation grow exponentially under varying road levels [26]. To further explain effect of different road levels on noise variance *Q* and state estimation of vehicle system, performance of proposed AUKF algorithm was validated under three conditions, i.e. level ISO-*A*, level ISO-*B* and level ISO-*C* road excitation.

Fig. 9 shows that the estimated sprung mass velocity, pitch rate, roll rate, rattle space of left front side, unsprung mass velocity of left front side and tire deflection of left front side under varying process noise variance *Q*. According to simulation results, better state estimation accuracy was observed when using corresponding *Q* and ***R*** values under different road excitation level. For sprung mass velocity of vehicle body and vehicle rattle space of left front side, the error of state estimation was obvious during measurement update process. Error values of state estimation were caused by UKF gain, and as road excitation level increased. However, for the pitch rate and roll rate of vehicle system, error in state estimation was not obvious under the same conditions. It may be related to state of vehicle movement [31]. Fig. 9 shows that state response accuracy of estimation is not better during the initial phase of using corresponding values of *Q*. It reduced accuracy may be caused by UKF gain during the short time interval of road level change. It can be concluded that when both *Q* and ***R*** are in correspondence, vehicle state estimation accuracy is the highest.

$$\mathbf{B}=\begin{bmatrix} \frac{-1}{m_b} & \frac{a}{I_{yy}} & \frac{-B_f}{2I_{xx}} & 0 & 0 & 0 & 0 & \frac{1}{m_{w1}} & 0 & 0 & 0 & 0 & 0 & 0 & 0 & 0 \\ \frac{-1}{m_b} & \frac{a}{I_{yy}} & \frac{B_f}{2I_{xx}} & 0 & 0 & 0 & 0 & 0 & \frac{1}{m_{w2}} & 0 & 0 & 0 & 0 & 0 & 0 & 0 \\ \frac{-1}{m_b} & \frac{-b}{I_{yy}} & \frac{-B_r}{2I_{xx}} & 0 & 0 & 0 & 0 & 0 & 0 & \frac{1}{m_{w3}} & 0 & 0 & 0 & 0 & 0 & 0 \\ \frac{-1}{m_b} & \frac{-b}{I_{yy}} & \frac{B_r}{2I_{xx}} & 0 & 0 & 0 & 0 & 0 & 0 & 0 & \frac{1}{m_{w4}} & 0 & 0 & 0 & 0 & 0 \end{bmatrix}^T;$$

$$\mathbf{\Gamma}=\begin{bmatrix} 0 & 0 & 0 & 0 & 0 & 0 & 0 & 0 & 0 & 0 & 0 & 0 & 0 & 0 & -1 & 0 \\ 0 & 0 & 0 & 0 & 0 & 0 & 0 & 0 & 0 & 0 & 0 & 0 & 0 & -1 & 0 & 0 \\ 0 & 0 & 0 & 0 & 0 & 0 & 0 & 0 & 0 & 0 & 0 & 0 & -1 & 0 & 0 & 0 \\ 0 & 0 & 0 & 0 & 0 & 0 & 0 & 0 & 0 & 0 & 0 & -1 & 0 & 0 & 0 & 0 \end{bmatrix}^T;$$

$$\mathbf{C}=\begin{bmatrix} C1 & C2 \\ C3 & C4 \end{bmatrix};$$

$$\mathrm{C1}=\begin{bmatrix} C_{11} & C_{12} & C_{13} & -\frac{k_{s1}}{m_b} & -\frac{k_{s2}}{m_b} & -\frac{k_{s3}}{m_b} & -\frac{k_{s4}}{m_b} \\ 0 & 1 & 0 & 0 & 0 & 0 & 0 \\ 0 & 0 & 1 & 0 & 0 & 0 & 0 \\ \frac{c_{p1}}{m_{w1}} & -\frac{a\cdot c_{p1}}{m_{w1}} & \frac{B_f\cdot c_{p1}}{2m_{w1}} & \frac{k_{s1}}{m_{w1}} & 0 & 0 & 0 \end{bmatrix};$$

$$C2=\begin{bmatrix} \frac{c_{p1}}{m_b} & \frac{c_{p2}}{m_b} & \frac{c_{p3}}{m_b} & \frac{c_{p4}}{m_b} & 0 & 0 & 0 & 0 \\ 0 & 0 & 0 & 0 & 0 & 0 & 0 & 0 \\ 0 & 0 & 0 & 0 & 0 & 0 & 0 & 0 \\ -\frac{c_{p1}}{m_{w1}} & 0 & 0 & 0 & -\frac{k_{t1}}{m_{w1}} & 0 & 0 & 0 \end{bmatrix};$$

$$C3=\begin{bmatrix} \frac{c_{p2}}{m_{w2}} & -\frac{a\cdot c_{p2}}{m_{w2}} & -\frac{B_f\cdot c_{p2}}{2m_{w1}} & \frac{k_{s2}}{m_{w2}} & 0 & 0 & 0 \\ \frac{c_{p3}}{m_{w3}} & \frac{b\cdot c_{p3}}{m_{w3}} & -\frac{B_r\cdot c_{p3}}{2m_{w3}} & 0 & 0 & \frac{k_{s3}}{m_{w3}} & 0 \\ \frac{c_{p4}}{m_{w4}} & \frac{a\cdot c_{p4}}{m_{w4}} & -\frac{B_r\cdot c_{p4}}{2m_{w4}} & 0 & 0 & 0 & \frac{k_{s4}}{m_{w4}} \end{bmatrix};$$

$$C4=\begin{bmatrix} -\frac{c_{p2}}{m_{w2}} & 0 & 0 & 0 & -\frac{k_{t2}}{m_{w2}} & 0 & 0 & 0 \\ 0 & 0 & -\frac{c_{p3}}{m_{w3}} & 0 & 0 & 0 & -\frac{k_{t3}}{m_{w3}} & 0 \\ 0 & 0 & 0 & -\frac{c_{p4}}{m_{w4}} & 0 & 0 & 0 & -\frac{k_{t4}}{m_{w4}} \end{bmatrix};$$

$$C_{11}=A_{11};\quad C_{12}=A_{12};\quad C_{13}=A_{13};$$

$$\mathbf{D}=\begin{bmatrix} \frac{-1}{m_b} & 0 & 0 & \frac{1}{m_{w1}} & 0 & 0 & 0 \\ \frac{-1}{m_b} & 0 & 0 & 0 & \frac{1}{m_{w2}} & 0 & 0 \\ \frac{-1}{m_b} & 0 & 0 & 0 & 0 & \frac{1}{m_{w3}} & 0 \\ \frac{-1}{m_b} & 0 & 0 & 0 & 0 & 0 & \frac{1}{m_{w4}} \end{bmatrix}^T$$

To further describe state estimation error, mean absolute error was utilized to estimate the accuracy of the AUKF approach. Based on analysis of Fig. 9, state estimation of sprung mass velocity, roll rate, pitch rate, rattle space of left front side, unsprung mass velocity of left front side and tire deflection of left front side were chosen to calculate mean absolute error. To conveniently estimate influence of estimation error on vehicle system's state estimation, simulation results are shown under road level ISO-*A*, ISO-*B*and ISO-*C* excitations. In Fig. 10, data for simulation results during

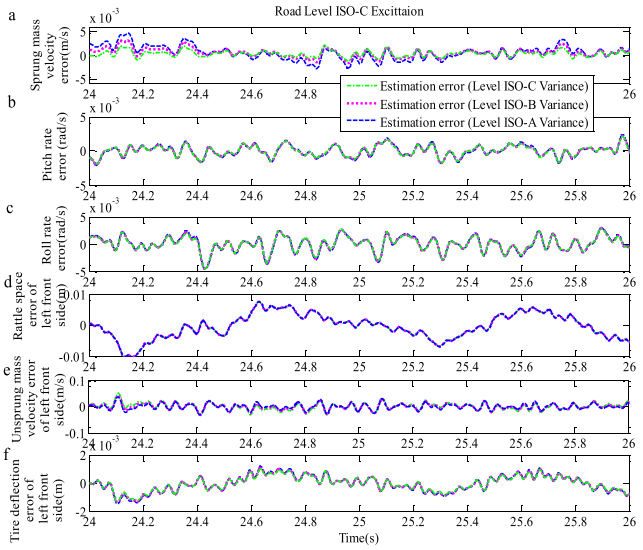

FIGURE 12. Error of state estimation for road level ISO-*C* excitation using level ISO-*A*/*B*/*C* process variance *Q* (a) Sprung mass velocity of vehicle body (b) Pitch rate (c) Roll rate (d) Rattle space of left front side (e) Unsprung mass velocity of left front side (f) Tire defection of left front side.

a time interval of two seconds (i.e. from $t = 4$ s to $t = 6$ s) is plotted under road level ISO-*A* excitation. Simulation results for a time interval of two seconds (i.e. from $t = 14$ s to $t = 16$ s) under road level ISO-*B* excitation is also plotted in Fig. 11. Data during a two second time interval (i.e. from $t = 24$ s to $t = 26$ s) under road level ISO-*C* excitation is shown in Fig. 12. Error value of state estimates compared to the reference value is not obvious for road level ISO-*A* excitation. However, increases are seen for level ISO-*B* and ISO-*C* excitations. For sprung mass velocity of vehicle body and unsprung mass velocity of left front side, influence of Q is obvious. This is because unsprung mass velocity of vehicle system and corresponding damper force are closely related an appropriate value of Q could be chosen for various road conditions.

Based on the above illustration, it can be seen that value of Q has a significant effect on vehicle state estimation, especially in cases of higher road excitation levels [24]. To further discuss estimation accuracy of the proposed AUKF approach, simulation data for the road level ISO-*A*, level ISO-*B*, and level ISO-*C* excitation under varying road level Q are listed in Table 5. Table 5 shows that there is a significant effect of Q used in AUKF algorithm on state estimation accuracy. State estimation accuracy can be increased using corresponding values of Q and $\boldsymbol{R}$ under various road excitation levels.

Based on the above discussion, it can be concluded that state estimation of the vehicle system is more accurate when matching values are used for different Q and $\boldsymbol{R}$ matrices under road level ISO-*A*, level ISO-*B*, and level ISO-*C* excitation conditions.

D. COMPARISON WITH EXISTING APPROACHES

To better illustrate the properties of the proposed AUKF method, comparisons with UKF method [16] was performed

TABLE 6. Estimation accuracy of different road excitation levels using different road process noise variance *Q*.

Method	Road level ISO-*A* Excitation		Road level ISO-*B* Excitation		Road level ISO-*C* Excitation	
	Accuracy of state estimation / %					
	$\dot{x}_b$	$\dot{x}_{w1}$	$\dot{x}_b$	$\dot{x}_{w1}$	$\dot{x}_b$	$\dot{x}_{w1}$
UKF	87	85	84	82	80	78
AUKF	95	94	93	90	91	90

in this section. The reason UKF method was selected due to the fact that UKF method represents basic nonlinear filter comes from current vehicle state.

The sprung mass velocity of vehicle body and unsprung mass velocity of left front side were selected to represent the proposed AUKF and UKF methods. Comparison results for a nominal vehicle model are shown in Table 6. Table 6 shows that higher accuracy can be obtained using the proposed AUKF method.

It should be note that more details about calculative accuracy can be found in [24].

According to the comparisons shown above, it can be concluded that the proposed method could outperform UKF method and is more robust to various driving conditions.

V. CONCLUSIONS

The AUKF algorithm is proposed to obtain higher accuracy in state estimation of a vehicle system under various road conditions in this paper.

The main contributions of the paper are as follows:

(1) Relationship between Q and $\boldsymbol{R}$ was comprehensively analyzed under different road excitation levels and imperative of Q on the vehicle state estimation was studied.
(2) A novel road classification approach through sprung mass acceleration and unsprung mass acceleration was used to accurately acquire Q of the vehicle system.
(3) The proposed AUKF approach was demonstrated to accurately estimate vehicle state under varying road excitations.

Finally, simulation data showed that the proposed AUKF algorithm can have higher accuracy of state estimation for a vehicle system, and was validated in MATLAB under road level ISO-*A*, level ISO-*B*, and level ISO-*C* excitation conditions.

In the future, a nonlinear vehicle model and road fault torlerant estimation will be considered. The proposed AUKF approach will be applied to actual road profiles under the controllable suspension will be carried out.

APPENDIX A

System matrix of state space equations (12-13).

$$\mathbf{A}=\begin{bmatrix}
A_{11} & A_{12} & A_{13} & A_{14} & A_{15} & A_{16} & A_{17} & A_{18} & A_{19} & A_{110} & A_{111} & 0 & 0 & 0 & 0\\
A_{21} & A_{22} & A_{23} & A_{24} & A_{25} & A_{26} & A_{27} & A_{28} & A_{29} & A_{210} & A_{211} & 0 & 0 & 0 & 0\\
A_{31} & A_{32} & A_{33} & A_{34} & A_{35} & A_{36} & A_{37} & A_{38} & A_{39} & A_{310} & A_{311} & 0 & 0 & 0 & 0\\
1 & -a & \frac{B_f}{2} & 0 & 0 & 0 & 0 & -1 & 0 & 0 & 0 & 0 & 0 & 0 & 0\\
1 & -a & -\frac{B_f}{2} & 0 & 0 & 0 & 0 & -1 & 0 & 0 & 0 & 0 & 0 & 0 & 0\\
1 & b & \frac{B_r}{2} & 0 & 0 & 0 & 0 & -1 & 0 & 0 & 0 & 0 & 0 & 0 & 0\\
1 & b & -\frac{B_r}{2} & 0 & 0 & 0 & 0 & -1 & 0 & 0 & 0 & 0 & 0 & 0 & 0\\
\frac{c_{p1}}{m_{w1}} & -\frac{c_{p1}\cdot a}{m_{w1}} & \frac{c_{p1}\cdot B_f}{2m_{w1}} & \frac{k_{s1}}{m_{w1}} & 0 & 0 & 0 & -\frac{c_{p1}}{m_{w1}} & 0 & 0 & 0 & -\frac{k_{t1}}{m_{w1}} & 0 & 0 & 0\\
\frac{c_{p2}}{m_{w2}} & -\frac{c_{p2}\cdot a}{m_{w2}} & -\frac{c_{p2}\cdot B_f}{2m_{w2}} & 0 & \frac{k_{s2}}{m_{w2}} & 0 & 0 & 0 & -\frac{c_{p2}}{m_{w2}} & 0 & 0 & 0 & -\frac{k_{t2}}{m_{w2}} & 0 & 0\\
\frac{c_{p3}}{m_{w3}} & \frac{c_{p3}\cdot b}{m_{w3}} & \frac{c_{p3}\cdot B_r}{2m_{w3}} & 0 & 0 & \frac{k_{s3}}{m_{w3}} & 0 & 0 & 0 & -\frac{c_{p3}}{m_{w3}} & 0 & 0 & 0 & -\frac{k_{t3}}{m_{w3}} & 0\\
\frac{c_{p4}}{m_{w4}} & \frac{c_{p4}\cdot b}{m_{w4}} & -\frac{c_{p4}\cdot B_r}{2m_{w4}} & 0 & 0 & 0 & \frac{k_{s4}}{m_{w4}} & 0 & 0 & 0 & -\frac{c_{p4}}{m_{w4}} & 0 & 0 & 0 & -\frac{k_{t4}}{m_{w4}}\\
0 & 0 & 0 & 0 & 0 & 0 & 0 & 1 & 1 & 1 & 1 & 0 & 0 & 0 & 0\\
0 & 0 & 0 & 0 & 0 & 0 & 0 & 1 & 1 & 1 & 1 & 0 & 0 & 0 & 0\\
0 & 0 & 0 & 0 & 0 & 0 & 0 & 1 & 1 & 1 & 1 & 0 & 0 & 0 & 0\\
0 & 0 & 0 & 0 & 0 & 0 & 0 & 1 & 1 & 1 & 1 & 0 & 0 & 0 & 0
\end{bmatrix}$$

$$A_{11}=-\frac{(c_{p1}+c_{p2}+c_{p3}+c_{p4})}{m_b};\quad A_{12}=\frac{a\cdot c_{p1}+a\cdot c_{p2}-b\cdot c_{p3}-b\cdot c_{p4}}{m_b};$$

$$A_{13}=\frac{-B_f\cdot c_{p1}+B_f\cdot c_{p2}-B_r\cdot c_{p3}+B_r\cdot c_{p4}}{2m_b};\quad A_{14}=-\frac{k_{s1}}{m_b};\quad A_{15}=-\frac{k_{s2}}{m_b};$$

$$A_{16}=-\frac{k_{s3}}{m_b};\quad A_{17}=-\frac{k_{s4}}{m_b};\quad A_{18}=\frac{c_{p1}}{m_b};\quad A_{19}=\frac{c_{p2}}{m_b};\quad A_{110}=\frac{c_{p3}}{m_b};\quad A_{111}=\frac{c_{p4}}{m_b};$$

$$A_{21}=\frac{a\cdot c_{p1}+a\cdot c_{p2}-b\cdot c_{p3}-b\cdot c_{p4}}{I_{yy}};\quad A_{22}=-\frac{a^2\cdot c_{p1}+a^2\cdot c_{p2}+b^2\cdot c_{p3}+b^2\cdot c_{p4}}{I_{yy}};$$

$$A_{23}=\frac{B_f\cdot a\cdot c_{p1}-B_f\cdot a\cdot c_{p2}-B_r\cdot b\cdot c_{p3}+B_r\cdot b\cdot c_{p4}}{2I_{yy}};\quad A_{24}=\frac{a\cdot k_{s1}}{I_{yy}};\quad A_{25}=\frac{a\cdot k_{s2}}{I_{yy}};$$

$$A_{26}=-\frac{b\cdot k_{s1}}{I_{yy}};\quad A_{27}=-\frac{b\cdot k_{s1}}{I_{yy}};\quad A_{28}=-\frac{a\cdot c_{p1}}{I_{yy}};\quad A_{29}=-\frac{a\cdot c_{p2}}{I_{yy}};\quad A_{210}=\frac{b\cdot c_{p1}}{I_{yy}};\quad A_{211}=\frac{b\cdot c_{p1}}{I_{yy}};$$

$$A_{31}=\frac{-B_f\cdot c_{p1}+B_f\cdot c_{p2}-B_r\cdot c_{p3}+B_r\cdot c_{p4}}{2I_{xx}};\quad A_{32}=\frac{B_f\cdot a\cdot c_{p1}-B_f\cdot a\cdot c_{p2}-B_r\cdot b\cdot c_{p3}+B_r\cdot b\cdot c_{p4}}{2I_{xx}};$$

$$A_{33}=-\frac{B_f^2\cdot c_{p1}+B_f^2\cdot c_{p2}+B_r^2\cdot c_{p3}+B_r^2\cdot c_{p4}}{4I_{xx}};\quad A_{34}=-\frac{B_f\cdot k_{s1}}{2I_{xx}};\quad A_{35}=\frac{B_f\cdot k_{s2}}{2I_{xx}};$$

$$A_{36}=-\frac{B_f\cdot k_{s3}}{2I_{xx}};\quad A_{37}=\frac{B_f\cdot k_{s4}}{2I_{xx}};\quad A_{38}=\frac{B_f\cdot c_{p1}}{2I_{xx}};\quad A_{39}=-\frac{B_f\cdot c_{p2}}{2I_{xx}};\quad A_{310}=\frac{B_r\cdot c_{p3}}{2I_{xx}};\quad A_{311}=-\frac{B_r\cdot c_{p4}}{2I_{xx}};$$

REFERENCES

[1] D. Cao, X. Song, and M. Ahmadian, "Editors' perspectives: Road vehicle suspension design, dynamics, and control," *Vehicle Syst. Dyn.*, vol. 49, nos. 1–2, pp. 3–28, 2011.

[2] A. Pazooki, S. Rakheja, and D. Cao, "Modeling and validation of off-road vehicle ride dynamics," *Mech. Syst. Signal Process.*, vol. 28, pp. 679–695, Apr. 2012.

[3] D. Cao, S. Rakheja, and C.-Y. Su, "Roll- and pitch-plane coupled hydro-pneumatic suspension," *Vehicle Syst. Dyn.*, vol. 48, no. 3, pp. 361–386, 2010.

[4] X. Jin and G. Yin, "Estimation of lateral tire–road forces and sideslip angle for electric vehicles using interacting multiple model filter approach," *J. Franklin Inst.*, vol. 352, no. 2, pp. 686–707, 2015.

[5] J. Chen, J. Song, L. Li, G. Jia, X. Ran, and C. Yang, "UKF-based adaptive variable structure observer for vehicle sideslip with dynamic correction," *IET Control Theory Appl.*, vol. 10, no. 14, pp. 1641–1652, 2016.

[6] B. Moaveni, M. K. R. Abad, and S. Nasiri, "Vehicle longitudinal velocity estimation during the braking process using unknown input Kalman filter," *Vehicle Syst. Dyn.*, vol. 53, no. 10, pp. 1373–1392, 2015.

[7] Y. Sun, L. Li, B. Yan, C. Yang, and G. Tang, "A hybrid algorithm combining EKF and RLS in synchronous estimation of road grade and vehicle' mass for a hybrid electric bus," *Mech. Syst. Signal Process.*, vols. 68–69, pp. 416–430, Feb. 2015, doi: 10.1016/j.ymssp.2015.08.015.

[8] K. Jiang, A. Victorino, and A. Charara, "Robust estimation of vehicle's dynamics states employing a parameter-variable EKF observer," in *Proc. IEEE 19th Int. Conf. Intell. Transp. Syst. (ITSC)*, Nov. 2016, pp. 2219–2224.

[9] R. E. Kalman, "A new approach to linear filtering and prediction problems," *Trans. ASME, D, J. Basic Eng.*, vol. 82, no. 1, pp. 35–45, 1960.

[10] K. T. Leung, J. F. Whidborne, D. Purdy, and A. Dunoyer, "A review of ground vehicle dynamic state estimations utilising GPS/INS," *Vehicle Syst. Dyn.*, vol. 49, nos. 1–2, pp. 29–58, 2011.

[11] X. Huang and J. Wang, "Real-time estimation of center of gravity position for lightweight vehicles using combined AKF–EKF method," *IEEE Trans. Veh. Technol.*, vol. 63, no. 9, pp. 4221–4231, Nov. 2014.

[12] L. Li, G. Jia, X. Ran, J. Song, and K. Wu, "A variable structure extended Kalman filter for vehicle sideslip angle estimation on a low friction road," *Vehicle Syst. Dyn.*, vol. 52, no. 2, pp. 280–308, 2014.

[13] S. Hong, T. Smith, F. Borrelli, and J. K. Hedrick, "Vehicle inertial parameter identification using extended and unscented Kalman filters," in *Proc. 16th Int. IEEE Annu. Conf. Intell. Transp. Syst. (ITSC)*, The Hague, The Netherlands, Oct. 2013, pp. 1436–1441.

[14] E. Hashemi, A. Kasaiezadeh, S. Khosravani, A. Khajepour, N. Moshchuk, and S.-K. Chen, "Estimation of longitudinal speed robust to road conditions for ground vehicles," *Vehicle Syst. Dyn.*, vol. 54, no. 8, pp. 1120–1146, 2016.

[15] K.-Z. Liu, J. Li, W. Guo, P.-Q. Zhu, and X.-H. Wang "Navigation system of a class of underwater vehicle based on adaptive unscented Kalman filter algorithm," *J. Central South Univ.*, vol. 21, no. 2, pp. 550–557, 2014.

[16] S. Hong, C. Lee, F. Borrelli, and J. K. Hedrick, "A novel approach for vehicle inertial parameter identification using a dual Kalman filter," *IEEE Trans. Intell. Transp. Syst.*, vol. 16, no. 1, pp. 151–161, Feb. 2015.

[17] H. B. Pacejia, *Tire and Vehicle Dynamics*. Oxford, U.K.: Butterworth-Heinemann, 2002.

[18] J. J. Rath, M. Defoort, H. R. Karimi, and K. C. Veluvolu, "Output feedback active suspension control with higher order terminal sliding mode," *IEEE Trans. Ind. Electron.*, vol. 64, no. 2, pp. 1392–1403, Feb. 2017.

[19] J. J. Rath, M. Defoort, and K. C. Veluvolu, "Rollover index estimation in the presence of sensor faults, unknown inputs, and uncertainties," *IEEE Trans. Intell. Transp. Syst.*, vol. 17, no. 10, pp. 2949–2959, Oct. 2016.

[20] D. Tan and C. Lu, "The influence of the magnetic force generated by the in-wheel motor on the vertical and lateral coupling dynamics of electric vehicles," *IEEE Trans. Veh. Technol.*, vol. 65, no. 6, pp. 4655–4668, Jun. 2016.

[21] E. Hashemi, M. Pirani, A. Khajepour, A. Kasaiezadeh, S.-K. Chen, and B. Litkouhi, "Corner-based estimation of tire forces and vehicle velocities robust to road conditions," *Control Eng. Pract.*, vol. 61, pp. 28–40, Apr. 2017.

[22] L. Li, Y. Lu, R. Wang, and J. Chen, "A three-dimensional dynamics control framework of vehicle lateral stability and rollover prevention via active braking with MPC," *IEEE Trans. Ind. Electron.*, vol. 64, no. 4, pp. 3389–3401, Apr. 2017.

[23] Y. Qin, C. Xiang, Z. Wang, and M. Dong, "Road excitation classification for semi-active suspension system based on system response," *J. Vibrat. Control*, vol. 1, no. 1, pp. 1–17, 2017, doi: 10.1177/1077546317693432.

[24] Z. Wang, M. Dong, Y. Qin, Y. Du, F. Zhao, and L. Gu, "Suspension system state estimation using adaptive Kalman filtering based on road classification," *Vehicle Syst. Dyn.*, vol. 55, no. 3, pp. 371–398, 2016, doi: 10.1080/00423114.2016.1267374.

[25] Y. Qin, F. Zhao, Z. Wang, L. Gu, and M. Dong, "Comprehensive analysis for influence of controllable damper time delay on semi-active suspension control strategies," *J. Vibrat. Acoust.*, vol. 139, no. 3, p. 031006, 2017, doi: 10.1115/1.4035700.

[26] *Mechanical Vibration—Road Surface Profiles—Reporting of Measured Data*, document ISO 8608-1995, 1995.

[27] R. Mehra, "On the identification of variances and adaptive Kalman filtering," *IEEE Trans. Autom. Control*, vol. AC-15, no. 2, pp. 175–184, Apr. 1970.

[28] T. Cui and C. Tellambura, "Power delay profile and noise variance estimation for OFDM," *IEEE Commun. Lett.*, vol. 10, no. 1, pp. 25–27, Jan. 2006.

[29] Y. Zhao, B. Liang, and S. Iwnicki, "Friction coefficient estimation using an unscented Kalman filter," *Vehicle Syst. Dyn.*, vol. 52, suppl. 1, pp. 220–234, 2014.

[30] J. Y. Wong, *Theory of Ground Vehicles*. Hoboken, NJ, USA: Wiley, 2001.

[31] Z.-F. Wang, M.-M. Dong, L. Gu, J.-J. Rath, Y.-C. Qin, and B. Bai, "Influence of road excitation and steering wheel input on vehicle system dynamic responses," *Appl. Sci.*, vol. 7, no. 6, p. 570, 2017, doi: 10.3390/app7060570.

ZHENFENG WANG received the M.E. degree in mechanical engineering from Yanshan University, China, in 2012. He is currently pursuing the Ph.D. degree with the Noise and Vibration Control Laboratory, Beijing Institute of Technology. From 2017 to 2018, he was with the University of Waterloo as a Visiting Scholar. He is involved in vehicle dynamics, state estimation, and modeling for suspension system. His research interests include vehicle dynamics, nonlinear state estimation, and controllable suspension system.

YECHEN QIN received the B.Sc. and Ph.D. degrees in mechanical engineering from the Beijing Institute of Technology, China, in 2010 and 2016, respectively. From 2013 to 2014, he was with Texas A&M University, College Station, TX, USA, as a Visiting Ph.D. Student. From 2017 to 2018, he was with the University of Waterloo as a Visiting Scholar. He currently holds a post-doctoral position with the Beijing Institute of Technology, China. His research interests include controllable suspension system, road estimation, and in wheel motor vibration control.

LIANG GU received the Ph.D. degree from the University of Science and Technology Beijing in 1993. He is currently a Professor with the Beijing Institute of Technology. His research areas include suspension system dynamics, controllable suspension system, damper design and modeling, and estimation and modeling for lightweight vehicles suspension system.

MINGMING DONG received the Ph.D. degree from the Beijing Institute of Technology in 2003. From 2017 to 2018, he was with the University of Wollongong as a Visiting Scholar. He is currently the Director of the Noise and Vibration Laboratory with the Beijing Institute of Technology. His research areas include suspension system dynamics, in wheel motor vibration control, modeling and estimation, and modeling for lightweight vehicles suspension system.